Chemical Science

ROYAL SOCIETY OF CHEMISTRY

EDGE ARTICLE

View Article Online
View Journal

Cite this: DOI: 10.1039/d5sc06284e

All publication charges for this article have been paid for by the Royal Society of Chemistry

A bioorthogonal-catalytic artificial antigen-presenting cell for chemo- and immuno-therapy

Zhengwei Liu,[ab] Wenting Zhang,[ac] Chuanqi Zhao,[ac] Mengyu Sun,[ac] Jinsong Ren [abc] and Xiaogang Qu *[abc]

Received 18th August 2025
Accepted 13th November 2025

DOI: 10.1039/d5sc06284e

rsc.li/chemical-science

Bioorthogonal prodrug activation has emerged as a promising strategy in tumor therapy. However, its clinical translation is hindered by limited therapeutic efficacy due to the complexity of tumors and heterogeneity of individuals. Herein, an artificial antigen-presenting cell (aAPC)-based biomimetic bioorthogonal catalyst is developed by encapsulating transition metal catalysts (TMCs) within lipid nanoparticles cloaked with dendritic cell membranes (LNP-Fe@dcM). By imitating key immune cell functions, LNP-Fe@dcM mediates a dual-mode antitumor response *via* catalytic prodrug activation and immunomodulation. Particularly, localized activation of a doxorubicin prodrug kills tumor cells and induces immunogenic cell death (ICD), thereby releasing tumor-associated antigens and priming personalized antitumor immunity. Concurrently, dendritic cell membrane-derived ligand–receptor interactions facilitate T cell activation and proliferation. This synergistic strategy enables efficient antigen presentation and robust immune activation. The presented approach offers a versatile paradigm for engineering catalytic aAPCs toward bioorthogonal cancer immunotherapy.

Introduction

Bioorthogonal reactions refer to biocompatible reactions that occur within complex biological environments without interfering with native biochemical processes.[1,2] Distinguished by their exceptional selectivity, efficiency and robustness, bioorthogonal reactions have played a significant role in manipulation of biological processes *in situ*. These methodologies have propelled advances in cell imaging, biomolecular regulation, and therapeutic applications.[3–6] Recently, bioorthogonal chemistry has garnered significant interest in prodrug activation, particularly in oncology, where it mitigates drug-associated side effects.[7–9] Transition-metal catalysts (TMCs) have emerged as powerful candidates for bioorthogonal reactions.[10,11] For instance, homogeneous Ru and Pd complexes have been utilized to activate proteins and drugs within living cells.[12] However, their applications are hindered by poor stability and low reaction kinetics in biological media. To circumvent these limitations, heterogeneous catalysts have been engineered by embedding active metal species within nanomaterials.[13–16] Additionally, given the complexity and metastasis characteristics of tumors, single-mode therapeutic strategies remain inadequate for effective tumor treatment.[17,18] Therefore, the development of novel bioorthogonal catalysts with enhanced reactivity and multifunctional therapeutic potential is imperative for advancing tumor therapy.

Cancer immunotherapy is regarded as an innovative therapeutic strategy by exploiting the intrinsic capacity of immune system to eradicate malignant cells.[19,20] As professional antigen-presenting cells (APCs), dendritic cells (DCs) serve as key orchestrators to stimulate antitumor immunity.[21,22] DCs efficiently internalize, process, and display tumor-associated antigens in the form of peptide-major histocompatibility complex (pMHC) assemblies on their surface.[23] Upon maturation, DCs engages naive T cells, initiating a robust cytotoxic response against tumor cells.[24–26] However, the immunosuppressive tumor microenvironment (TME) frequently impairs DC activation and antigen presentation.[25] To circumvent these limitations, artificial antigen-presenting cells (aAPCs) have been developed as synthetic alternatives to natural APCs.[22,27] These engineered nanoscale constructs, especially cell membrane of APCs, are functionalized with biomimetic signaling proteins and ligands to facilitate antigen presentation. Unlike endogenous APCs, aAPCs maintain sustained functionality while providing superior stability and an extended lifespan. However, given the pronounced heterogeneity of cancers, it's a great challenge to construct aAPCs with abundant and personalized antigen expression. Therefore, integrating aAPCs with bioorthogonal catalysis-mediated ICD offers a promising strategy for effective cancer therapy.

Considering these points, we have developed an aAPC-based bioorthogonal catalyst by integrating TMCs into lipid nanoparticles (LNPs) coated with DC membranes (LNP-Fe@dcM).

[a]*Laboratory of Chemical Biology, State Key Laboratory of Rare Earth Resource Utilization, Changchun Institute of Applied Chemistry, Chinese Academy of Sciences, Changchun 130022, P. R. China. E-mail: xqu@ciac.ac.cn*
[b]*University of Chinese Academy of Sciences, Beijing 100039, P. R. China*
[c]*University of Science and Technology of China, Hefei, Anhui 230029, P. R. China*

LNPs serve as ideal nanocarriers due to their great biocompatibility and prolonged circulation time. Their rapid deployment in mRNA vaccine platforms during the COVID-19 pandemic further underscores their potential in biomedical applications.[28–30] With DC membrane cloaking, the designed LNP-Fe@dcM catalysts exhibit dual therapeutic functions (Scheme 1). Firstly, the embedded Fe catalyst mediates *in situ* activation of a doxorubicin (DOX) prodrug *via* bioorthogonal catalysis to eliminate tumor cells by inducing immunogenic cell death (ICD). This process concurrently releases personalized tumor-associated antigens (TAAs) to promote DC priming and robust antitumor immunity. Moreover, LNP-Fe@dcM directly supports T cell activation and proliferation through membrane-derived ligand–receptor interactions, involving MHC, CD40, CD86, and so on with their cognate receptors on T cells. This multifunctional platform enables both antigen generation and immune activation, thereby enhancing immunotherapeutic efficacy. The work offers a versatile framework for engineering bioorthogonally active aAPCs for advanced cancer immunotherapy.

Materials and methods

Preparations of FeTPPCl LNPs

To prepare the FeTPPCl LNPs, DSPC was mixed with cholesterol and DSPE-PEG2000 at a mole ratio of 56.4 : 38.3 : 5.3, as well as different amount of FeTPPCl. The mass ratios of FeTPPCl to total lipid were 5%, 10% and 20%. Solvent was evaporated at 65 °C under a stream of nitrogen gas, followed by further drying under vacuum overnight. The thin film was then hydrated with PBS at 60 °C for 10 min or indicated time with gentle pipetting to form LNPs. LNPs were extruded 20 times through polycarbonate filters of 200 nm pore size to adjust size. Formulations were then transferred to a dialysis bag dialyzed against PBS to remove free FeTPPCl.

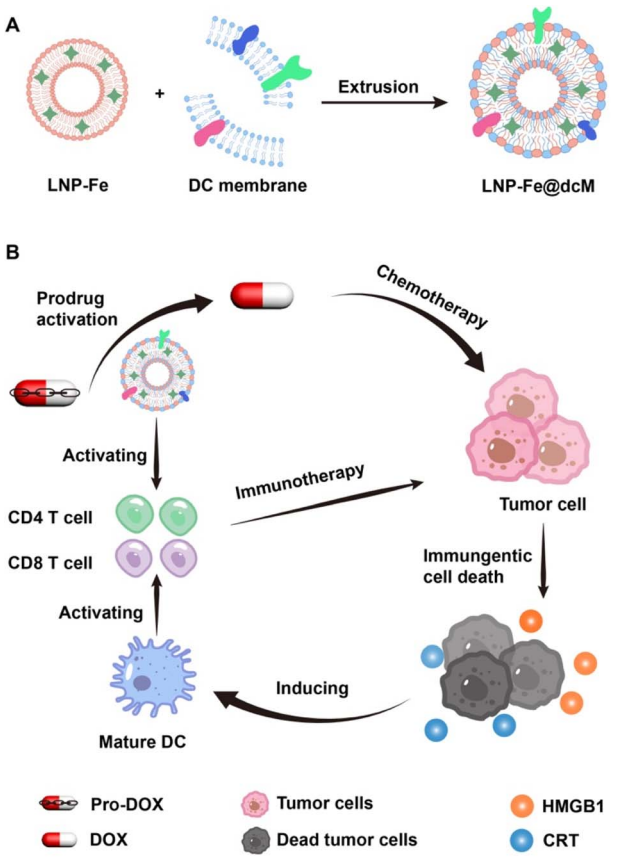

Scheme 1 Construction and function of LNP-Fe@dcM. (A) Illustration of constructing LNP-Fe@dcM. (B) Illustration of LNP-Fe@dcM-mediated prodrug activation and immune regulation for tumor killing.

Preparation of mouse bone marrow-derived dendritic cells (BMDCs)

Bone marrow cells were isolated from mouse femurs by flushing with RPMI-1640 medium and filtering through a 200-mesh sieve. Red blood cells were removed using RBC lysis buffer (Beyotime). After washing, cells were seeded in six-well plates and cultured in RPMI-1640 supplemented with 10% FBS, 1% penicillin-streptomycin, 20 ng mL^{-1} GM-CSF, and 10 ng mL^{-1} IL-4 at 37 °C with 5% CO_2. The medium was refreshed on days 3 and 5. On day 6, semi-adherent and non-adherent cells were harvested as immature BMDCs and further stimulated with lysed 4T1 cells, IFN-γ (100 ng mL^{-1}), and LPS (1 μg mL^{-1}) for 24 h to obtain mature BMDCs.

Preparation of mature BMDCs membranes

Mature BMDCs were harvested, washed three times with cold PBS, and centrifuged at 1000 rpm to remove residual medium. The cell suspensions were subjected to repeated freeze–thaw cycles in a buffer containing a membrane protein extraction reagent and phenylmethylsulfonyl fluoride (PMSF, Beyotime) according to the manufacturer's instructions and centrifuged at 700×*g* for 10 min at 4 °C to remove nuclei and intact cells. The supernatant was further centrifuged at 14 000×*g* for 30 min to collect the cell membrane fraction. The isolated membranes were lyophilized overnight and stored at −80 °C.

Preparation of LNP-Fe@dcM

The dcM from DCs was mixed with FeTPPCl LNPs with the overall protein: lipid ratio of 1 : 200 (by weight) and extruded through a polycarbonate membrane with pore sizes of 400 and 200 nm to prepare LNP-Fe@dcM.

Catalytic reduction of azide group mediated by LNP-Fe@dcM

The catalytic activity of LNP-Fe@dcM was evaluated by the cleavage of Pro-rhodamine 110 (Pro-Rh110, 3). Briefly, the LNP-Fe@dcM or other catalyst in described concentration were mixed with 10 μM Pro-Rh110 (20 mM in DMSO) and 2 mM sodium ascorbate (NaAsc, 50 mM in PBS) at 37 °C. After the indicated time, the fluorescence of different groups was recorded by fluorescence spectrometer. The conversion rate was quantified using the standard curve of Rh110. The reactions in different media were carried out using the same method.

LNP-Fe@dcM induced Pro-Rh110 deprotection in living cells

10 μM LNP-Fe@dcM (calculated based on Fe content), 20 μM Pro-Rh110 were incubated with pre-seeded cells. All groups were treated with 2 mM NaAsc except control in the meantime. After 24 h, the media were discarded, and cells were rinsed with PBS to remove LNP-Fe@dcM and extra Pro-Rh110. Then the generated fluorescent Rh110 in cells was monitored by flow cytometry. For fluorescence imaging, the nuclei were stained with DAPI. The fluorescence image was obtained by OLYMPUS-BX51 microscopes.

Cytotoxicity test of LNP-Fe@dcM mediated Pro-DOX activation

4T1 cells were placed in 96-well plates (1×10^4 cells per well) and cultured overnight. LNP-Fe@dcM with different concentrations (0, 3.8, 7.5, 15 and 30 μM) was added to the wells for 24 h for material biosafety test. Moreover, different concentrations (7.5 and 15 μM) of LNP-Fe@dcM were incubated with Pro-DOX at indicated concentrations (2 μM). PBS was used in control group. Following a 3-day incubation, 10 μL of Cell Counting Kit-8 (CCK-8) reagent was added to each well, and the cells were incubated for an additional 2 h. The absorbance at 450 nm was subsequently recorded using a microplate reader.

Live/dead assay

The 4T1 cells were seeded in 24-well. After one night growth, the cells were treated with PBS as control, LNP-Fe@dcM, Pro-DOX, LNP-Fe@dcM + Pro-DOX, or DOX, respectively. The LNP-Fe@dcM was 7.5 μM. The DOX and Pro-DOX were 2 μM. All groups were treated with 2 mM NaAsc except control. 48 h later, calcein AM and PI were used to detect the viability of cells by fluorescence imaging.

Cell apoptosis assays

4T1 cells were seeded in 6-well plates (1×10^6 cells per well). After one night growth, the cells were treated with PBS as control, LNP-Fe@dcM, Pro-DOX, LNP-Fe@dcM + Pro-DOX, or DOX, respectively. The LNP-Fe@dcM was 7.5 μM. The DOX and Pro-DOX were 2 μM. All groups were treated with 2 mM NaAsc except control in the meantime. After 48h, cells were collected and stained by Annexin V-FITC/PI apoptosis detection kit for flow cytometer analysis.

In vivo treatment in 4T1 breast cancer model

For the *in vivo* therapeutic study, the 4T1 orthotopic tumor model was created through implanting 1×10^6 4T1 tumor cells into right mammary fat pads of BALB/c mice. The mice were treated following ten days of tumor growth.

4T1 tumor-bearing mice were randomly divided into 5 groups: (1) PBS, (2) Pro-DOX, (3) LNP-Fe@dcM, (4) Pro-DOX + LNP-Fe, (5) Pro-DOX + LNP-Fe@dcM. According to the therapeutic schedule, mice were injected intravenously with LNP-Fe@dcM or LNP-Fe (10 mg kg^{-1}). Then Pro-DOX (8 mg kg^{-1}) and NaAsc (100 mg kg^{-1}) was injected intraperitoneally after 12 h, respectively. The treatments were performed every 3 days, 3 rounds in total. Tumor sizes and body weights of mice were recorded every three days. Tumor volume = 1/2 × (length × width^2). At last, mice were sacrificed, and the tumors and major organs were gathered for further study.

Lung metastasis model

The mice were inoculated with tumor and grew 10 days, followed by 3-round treatment: (1) PBS, (2) Pro-DOX, (3) Pro-DOX + LNP-Fe, (4) Pro-DOX + LNP-Fe@dcM. Next, the residual 4T1 tumor mass was surgically removed. Then mice were challenged with 5×10^5 4T1 tumor cells *via* tail vein injection to establish the lung metastasis model. After 21 days, lungs were collected for observation. In addition, lung sections were obtained from each group and further studied by H&E staining assay.

Evaluation of antitumor immune response

For immunofluorescence staining, the harvested tumor tissues were embedded, frozen, and sectioned into 8-μm-thick slices. The sections were incubated with anti-CD8 primary antibody overnight at 4 °C, followed by incubation with the corresponding secondary antibody and counterstaining with DAPI. Fluorescence signals were visualized using a confocal laser scanning microscope.

For flow cytometry analysis, lymph nodes were collected, mechanically dissociated using a syringe plunger, and passed through a 200-mesh cell strainer to obtain single-cell suspensions. The cells were washed three times with cold PBS (pH 7.4) and resuspended in 100 μL PBS (10^6 cells). The maturation of DCs in lymph nodes was determined by staining with anti-CD11c, anti-CD86, and anti-CD80 antibodies according to the manufacturer's instructions.

Results and discussion

To verify our design, we constructed DC membrane-coated FeTPPCl LNPs through the following steps: preparing FeTPPCl LNPs, collecting DC membranes, then camouflaging FeTPPCl LNPs with DC membranes. Specifically, FeTPPCl LNPs were formulated using different lipids and FeTPPCl.[31] Different mass ratios of FeTPPCl were loaded in the LNPs to determine the optimal ratio for subsequent applications. When the FeTPPCl mass ratio reached 20%, the LNPs aggregated within 24 hours (Fig. S1A). But the stability of LNPs was hardly affected when the mass ratios of FeTPPCl were 5% and 10%. Thus, LNPs with a 10% FeTPPCl were selected for further studies. And ICP analysis identified the loading capacity as 3.8%. Transmission electron microscopy revealed that the FeTPPCl LNPs were nanometer-sized (Fig. 1A). The hydrodynamic diameter was around 130 nm according to Fig. S1B. The size of LNPs remained stable in phosphate-buffered saline (PBS, pH 7.4) for 24 hours (Fig. S1B). In addition, Fig. S1C showed that FeTPPCl remained stably encapsulated in the LNPs with negligible leakage over 72 h. Furthermore, we examined the effect of different PBS incubation time on the characteristics of the generated LNPs. When the incubation time was extended to 20 min, the particle size slightly increased when compared to

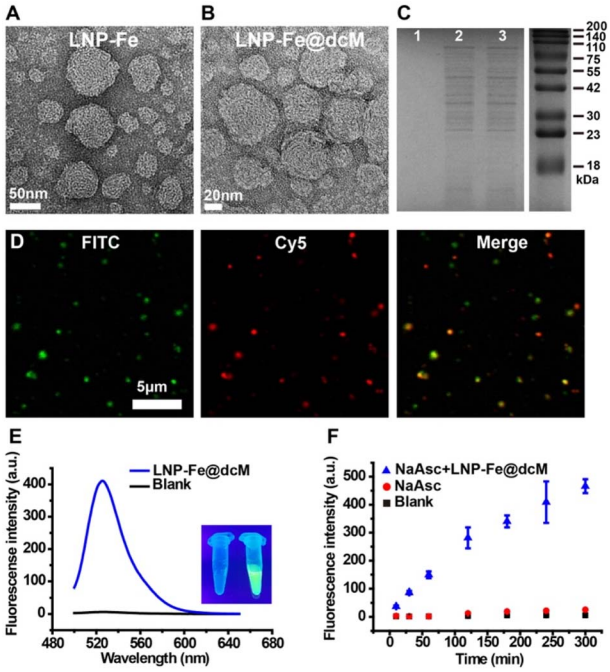

Fig. 1 Characterization and catalytic activity of LNP-Fe@dcM. (A) Transmission electron microscopy picture of LNP-Fe. (B) Transmission electron microscopy picture of LNP-Fe@dcM. (C) Protein profiles in (1): LNP-Fe, (2): dcM, and (3): LNP-Fe@dcM characterized by SDS-PAGE. (D) Confocal laser scanning microscopy pictures of LNP-Cy5@dcM. DC membrane labeled with fluorescein isothiocyanate (FITC) (green). LNP encapsulated with Cy5 dye (red). (E) Fluorescence enhancement of Pro-Rh110, 3 upon 4 h incubation with LNP-Fe@dcM and sodium ascorbate. Insert: representative images of the corresponding reaction mixtures. Left, Pro-Rh110 without treatment. Right, Pro-Rh110 treated with LNP-Fe@dcM. Both groups were treated with sodium ascorbate. (F) Fluorescence intensity of the produced fluorescent Rh110 when Pro-Rh110 was treated differently at certain time points.

10 min incubation, but the difference was not statistically significant (Fig. S2A). When prolonged to 30 min, the particle size became significantly larger than the 10 min group. In addition, no significant differences in PDI or FeTPPCl loading capacity were observed among these groups (Fig. S2B and C). These results indicated that a 10 min incubation provided optimal size control without compromising loading efficiency. Next, DC membrane fragments (dcM) were obtained from mature mouse bone marrow derived-dendritic cells (BMDCs) treated with 4T1 cell lysate, IFN-γ and LPS (Fig. S3). The elevated expression of MHC II, CD40 and CD86 markers on DC membranes would play a significant role in T cell activation and proliferation.[32,33] Self-assembly of dcM onto the LNP surface was facilitated by repeated extrusion, yielding cell membrane-fused FeTPPCl LNPs (termed LNP-Fe@dcM, Fig. 1B).[5,34] ICP analysis determined the FeTPPCl mass fraction in LNP-Fe@dcM to be 2.7%. Multiple characterizations confirmed the successful membrane camouflage around LNP-Fe. Sodium dodecyl sulfate-polyacrylamide gel electrophoresis (SDS-PAGE) verified the retention of membrane proteins in LNP-Fe@dcM (Fig. 1C). Additionally, colocalization analysis confirmed that LNP was successfully cloaked by dcM (Fig. 1D). Fig. S1D suggested that the LNP-Fe@dcM had good stability in PBS for 24 h.

To assess the catalytic activity, we synthesized pro-rhodamine 110 (Pro-Rh110, 3), which exhibited quenched fluorescence due to the presence of an azide group according to our previous method.[35] Upon incubation with the LNP-Fe@dcM catalyst, the fluorescence of rhodamine 110 (Rh110, 4) was restored (Fig. S4A). As shown in Fig. 1E, compound 3 displayed minimal fluorescence around 530 nm, confirming the effective caging of Pro-Rh110. Upon treatment with LNP-Fe@dcM, fluorescence intensity was significantly enhanced compared to the control group (Fig. 1E). What's more, a distinct green fluorescence was observed in the test tube, verifying the catalytic activity (Fig. 1E). These data confirmed the successful construction of the LNP-Fe@dcM catalyst. Additionally, as illustrated in Fig. S4B, the catalytic activity was dependent on the catalyst concentration. Time-dependent analysis further demonstrated the progressive increase in fluorescence intensity (Fig. 1F). Based on the Rh110 standard curve, the conversion rate of Pro-Rh110 reached approximately 52.0% at 300 minutes. We further compared the catalytic performance of LNP-Fe@cM and free FeTPPCl in various biological media. LNP-Fe@cM exhibited superior catalytic activity over free FeTPPCl in both PBS and FBS (Fig. S5). These results demonstrated that LNP-Fe@cM effectively stabilized the transition-metal catalyst, overcoming the inherent instability of homogeneous TMCs under physiological conditions.

After confirming the catalytic activity of LNP-Fe@dcM in solution, we proceeded to evaluate its performance at cellular level. At first, the cytotoxicity results demonstrated the good biocompatibility of LNP-Fe@dcM (Fig. S6). Next, fluorescence imaging revealed the obvious fluorescence signals were observed in cells treated with Pro-Rh110 + LNP-Fe@dcM rather than Pro-Rh110 alone (Fig. 2A). Flow cytometry analysis further showed that cells exposed to Pro-Rh110 + LNP-Fe@dcM exhibited approximately 15.7-fold higher fluorescence intensities than those without LNP-Fe@dcM (Fig. 2B). These findings highlighted the ability of LNP-Fe@dcM to catalyze bioorthogonal reactions in living cells, demonstrating its potential for the *in situ* generation of therapeutic compounds.

Subsequently, we examined whether LNP-Fe@dcM could facilitate bioorthogonal activation of the chemotherapeutic doxorubicin (DOX) prodrug and induce tumor cell death. For this purpose, we designed an aryl azide carbamate-caged DOX (Pro-DOX), which prevented cytotoxicity by blocking DNA binding and enzyme-mediated DNA damage.[35] As shown in Fig. S7, Pro-DOX alone exhibited minimal toxicity at 2 μM. In contrast, tumor cells treated with 7.5 μM or 15 μM LNP-Fe@dcM catalysts and 2 μM Pro-DOX exhibited significant cell death. The lowest cell viability reached 9.3%. Live/dead staining further confirmed extensive cell death in LNP-Fe@dcM + Pro-DOX group, which was comparable to cells treated with DOX (Fig. 3A). To quantify apoptosis, tumor cells were stained with Annexin V-FITC/PI and analyzed by flow cytometry. As shown in Fig. 3B, treatment with Pro-DOX + LNP-Fe@dcM led to a pronounced tumor cell killing performance, with an apoptosis rate of 33.0%. Whereas LNP-Fe@dcM or Pro-DOX alone

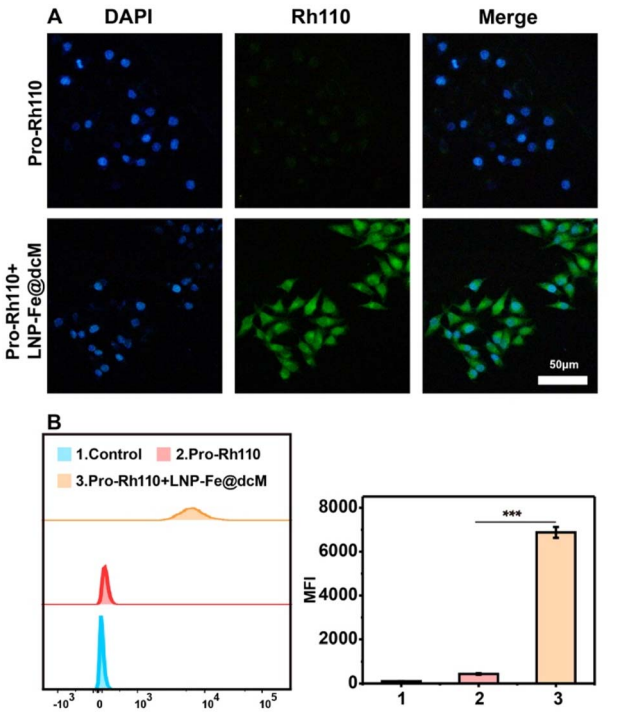

Fig. 2 Bioorthogonal deprotection of Pro-Rh110 catalyzed by LNP-Fe@dcM in cells. (A) The deprotection of Pro-Rh110 catalyzed by LNP-Fe@dcM in 4T1 cells. (B) Flow cytometry and quantitative analysis of 4T1 cells incubated with various treatments. Data are shown as mean ± SD, $n = 3$. *P <0.05, **P <0.01, and ***P <0.001.

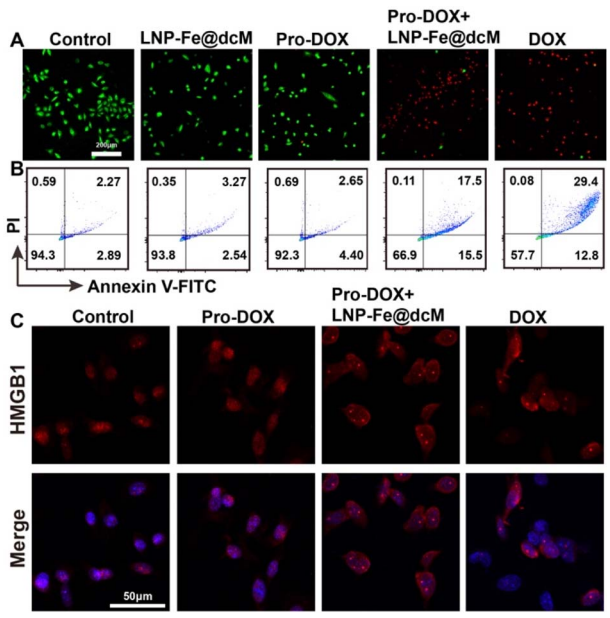

Fig. 3 Bioorthogonal activation of Pro-DOX for tumor cell eradication. (A) Live/dead staining of 4T1 cells following various treatments. Scale bar = 200 μm. (B) Annexin V-fluorescein and propidium iodide (PI) staining to assess apoptosis in differently treated 4T1 cells. (C) Immunofluorescence staining by ICD marker HMGB1 (red) after different treatments. Nuclei were stained with DAPI (blue). All groups were treated with sodium ascorbate except control in the meantime.

negligibly resulted in cell apoptosis. These findings demonstrated the enhanced tumor cell killing through LNP-Fe@dcM-mediated prodrug activation.

Anthracyclines, such as DOX, are known to induce an immunological response through the process of immunogenic cell death (ICD), which is characterized by the release of high-mobility group box 1 (HMGB1) and the surface exposure of calreticulin (CRT).[36,37] These molecules function as 'eat me' and danger-associated signals, enhancing antigen presentation by dendritic cells and promoting the activation of cytotoxic T lymphocytes. We thus investigated whether LNP-Fe@dcM-induced activation of Pro-DOX could trigger ICD. Immunofluorescence assays confirmed the release of HMGB1 from the nucleus (Fig. 3C). To further validate ICD induction, we examined CRT exposure. As shown in Fig. S8, robust red fluorescence was detected in the LNP-Fe@dcM + Pro-DOX group, indicating significant CRT translocation to the cell membrane of 4T1 cells. These results provided compelling evidence of bioorthogonal cleavage of Pro-DOX to effectively trigger ICD.

Prior to evaluating the *in vivo* antitumor efficacy of LNP-Fe@dcM, we first assessed their biosafety to confirm their suitability for *in vivo* applications. The serum biochemical parameters of mice were tested to evaluate the biosafety of the designed LNP-Fe@dcM. Seven days after LNP-Fe@dcM treatment, serum levels of key biomarkers, including alanine aminotransferase (ALT), aspartate aminotransferase (AST), total protein (TP), albumin (ALB), globulin (GLOB), blood urea nitrogen (BUN), creatinine (CREA), uric acid (UA) and CO_2, were measured to assess liver and kidney function. All parameters remained within normal physiological ranges, indicating that LNP-Fe@dcM did not induce detectable hepatic or renal toxicity (Fig. S9A and B). Furthermore, hematoxylin and eosin (H&E) staining of major organs revealed no noticeable histopathological alterations after treatment with LNP-Fe@dcM at both 7 and 28 days, indicating good biocompatibility of the formulation (Fig. S9C). To assess the *in vivo* antitumor performance of LNP-Fe@dcM, 4T1 orthotopic tumor model was established in BALB/c mice (Fig. 4A), followed by random assignment of the tumor-bearing mice into five groups: (1) PBS, (2) Pro-DOX, (3) LNP-Fe@dcM, (4) Pro-DOX + LNP-Fe, and (5) Pro-DOX + LNP-Fe@dcM. Tumor sizes were measured every three days. As shown in Fig. 4B, tumors in the PBS and Pro-DOX groups grew rapidly, indicating that Pro-DOX alone had minimal tumor inhibitory effects. The LNP-Fe@dcM group exhibited moderate tumor suppression. This performance could be attributed to the presence of co-stimulatory molecules (such as CD86 and CD40) and 4T1 tumor-associated antigens on the coating DC membrane to mediate T cell activation and proliferation. The Pro-DOX + LNP-Fe group exhibited apparent tumor suppression, suggesting bioorthogonal activation of Pro-DOX could effectively suppress tumor development. Compared with Pro-DOX + LNP-Fe group and other groups, the Pro-DOX + LNP-Fe@dcM group displayed a significant reduction in tumor growth, highlighting the therapeutic potential of *in situ* drug generation and synergistic immunotherapy. To further elucidate the mechanism underlying tumor suppression induced by the bioorthogonal catalytic platform, DCs in lymph nodes were

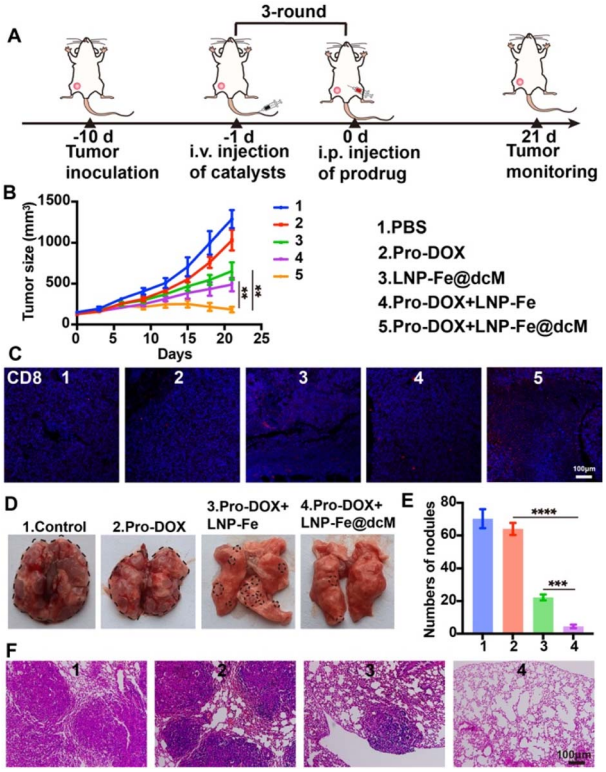

Fig. 4 LNP-Fe@dcM for *in vivo* 4T1 tumor therapy and suppression of lung metastasis. (A) Schematic illustration of the therapeutic regimen using LNP-Fe@dcM in 4T1 tumor-bearing BALB/c mice. i.v., intravenous; i.p., intraperitoneal. (B) Tumor growth curves of mice treated with the indicated formulations. Data are presented as mean ± SD (n = 5). (C) Immunofluorescence staining of $CD8^+$ T cells in tumor sections. Nuclei were counterstained with DAPI (blue). (D) Representative images of lung tissues from the respective treatment groups. The metastatic lung nodules were indicated with circles. (E) Quantification of metastatic lung nodules in (D). Data are shown as mean ± SD (n = 3). (F) H&E-stained sections of lung tissues from mice receiving different treatments. Asterisks indicated significant differences (*P < 0.05, **P < 0.01, ***P < 0.001).

stained for flow cytometry analysis. Based on Fig. S10, the mature DC cells from mice treated with Pro-DOX + LNP-Fe@dcM increased, higher than monotherapy treatment, demonstrating the effective activation of the anti-tumor immune response. Since $CD8^+$ T cells play a pivotal role in tumor eradication and immune modulation, their presence within tumor tissues was assessed. In Fig. 4C, we observed the elevated level of tumor infiltrating $CD8^+$ T cells in LNP-Fe@dcM alone treated group when compared to control group or Pro-DOX group or Pro-DOX + LNP-Fe group, validating the T cell proliferation within tumors mediated by the designed DC membrane coating. The most tumor infiltrating $CD8^+$ T cells were detected in Pro-DOX + LNP-Fe@dcM treated group, indicating the efficient T cell proliferation within tumors mediated by bioorthogonal catalysis-induced ICD and DC membrane coating (Fig. 4C). Taken together, these results highlighted the potent therapeutic synergy between bioorthogonal reaction-mediated chemotherapy and immunotherapy.

In addition to eliciting a potent immune response, we further investigated whether LNP-Fe@dcM could suppress tumor metastasis. In a tumor metastasis model, treated mice were intravenously rechallenged with 4T1 tumor cells. As shown in Fig. 4D and E, lung tissues from the Pro-DOX-treated group exhibited numerous metastatic nodules, whereas mice receiving LNP-Fe@dcM alone showed a markedly reduced metastatic burden. This effect was likely attributed to the immune activation triggered by the antigen-presenting capability of LNP-Fe@dcM. Notably, the Pro-DOX + LNP-Fe@dcM-treated group displayed minimal metastatic lesions. Histological analysis *via* H&E staining further supported these observations (Fig. 4F). Collectively, these findings indicated that LNP-Fe@dcM-based chemoimmunotherapy effectively eliminated primary tumors and provided protection against tumor rechallenge-induced lung metastasis.

Conclusions

In summary, we have developed a bioorthogonal catalytic aAPC by incorporating TMCs into lipid nanoparticles cloaked with DC membranes. Leveraging TMC-mediated catalysis, LNP-Fe@dcM enables *in situ* prodrug activation to eliminate tumors and induce ICD. The released tumor-associated antigens promote dendritic cell maturation and initiate personalized antitumor immunity. Additionally, LNP-Fe@dcM directly stimulates T cell activation and proliferation *via* ligand–receptor interactions on its surface. Notably, treatment with Pro-DOX + LNP-Fe@dcM leads to a marked increase in intratumoral $CD8^+$ T cell infiltration. This study presents a versatile strategy for engineering catalytic aAPCs and underscores the potential of LNP-based bioorthogonal systems in next-generation cancer immunotherapy.

Ethical statement

All animal experiments were performed in accordance with the guidelines for the care and use of laboratory animals and approved by the Ethics Committee for Animal Experimentation of Changchun Institute of Applied Chemistry, Chinese Academy of Sciences.

Author contributions

J. R. and X. Q. designed research; Z. L., and W. Z. performed research; Z. L. C. Zhao, and M. S. analysed data; Z. L. and X. Q. wrote the paper.

Conflicts of interest

All authors declare no competing interests.

Data availability

The data available upon reasonable request from the authors.

Supplementary information is available. See DOI: **https://doi.org/10.1039/d5sc06284e**.

Acknowledgements

Financial support was provided by the National Key R&D Program of China (2022YFA1205804), and National Natural Science Foundation of China (T249526, 2243700, 2223700, 22207102).

References

1 Z. Liu, M. Sun, W. Zhang, J. Ren and X. Qu, *Angew. Chem., Int. Ed.*, 2023, **62**, e202308396.
2 S. Fedeli, J. Im, S. Gopalakrishnan, J. L. Elia, A. Gupta, D. Kim and V. M. Rotello, *Chem. Soc. Rev.*, 2021, **50**, 13467–13480.
3 H. Wang and D. J. Mooney, *Nat. Chem.*, 2020, **12**, 1102–1114.
4 Y. Zhu, L. I. Willems, D. Salas, S. Cecioni, W. B. Wu, L. J. Foster and D. J. Vocadlo, *J. Am. Chem. Soc.*, 2020, **142**, 15729–15739.
5 Z. Liu, F. Wang, X. Liu, Y. Sang, L. Zhang, J. Ren and X. Qu, *Proc. Natl. Acad. Sci. U. S. A*, 2021, **118**, e2022769118.
6 W. Zhang, J. Zhu, J. Ren and X. Qu, *Adv. Mater.*, 2024, e2405318.
7 H. Zhao, Y. Zhang, Y. Sun, Z. Zhu, J. Ren and X. Qu, *Angew. Chem., Int. Ed.*, 2025, e202425018.
8 Z. Cao, D. Li, L. Zhao, M. Liu, P. Ma, Y. Luo and X. Yang, *Nat. Commun.*, 2022, **13**, 2038.
9 W. Wang, X. Zhang, R. Huang, C.-M. Hirschbiegel, H. Wang, Y. Ding and V. M. Rotello, *Adv. Drug Delivery Rev.*, 2021, 113893.
10 Y. Bai, J. Chen and S. C. Zimmerman, *Chem. Soc. Rev.*, 2018, **47**, 1811–1821.
11 J. Li and P. R. Chen, *Nat. Chem. Biol.*, 2016, **12**, 129–137.
12 T. Völker, F. Dempwolff, P. L. Graumann and E. Meggers, *Angew. Chem., Int. Ed.*, 2014, **53**, 10536–10540.
13 F. Wang, Y. Zhang, Z. Liu, Z. Du, L. Zhang, J. Ren and X. Qu, *Angew. Chem., Int. Ed.*, 2019, **58**, 6987–6992.
14 A. M. Pérez-López, B. Rubio-Ruiz, V. Sebastián, L. Hamilton, C. Adam, T. L. Bray, S. Irusta, P. M. Brennan, G. C. Lloyd-Jones, D. Sieger, J. Santamaría and A. Unciti-Broceta, *Angew. Chem., Int. Ed.*, 2017, **56**, 12548–12552.
15 J. T. Weiss, J. C. Dawson, K. G. Macleod, W. Rybski, C. Fraser, C. Torres-Sanchez, E. E. Patton, M. Bradley, N. O. Carragher and A. Unciti-Broceta, *Nat. Commun.*, 2014, **5**, 3277.
16 Y. You, Q. Deng, Y. Wang, Y. Sang, G. Li, F. Pu, J. Ren and X. Qu, *Nat. Commun.*, 2022, **13**, 1459.
17 J.-L. Liang, G.-F. Luo, W.-H. Chen and X.-Z. Zhang, *Adv. Mater.*, 2021, e2007630.
18 M. Chang, Z. Hou, M. Wang, C. Li and J. Lin, *Adv. Mater.*, 2020, e2004788.
19 C. Zhang, M. Xu, Z. Zeng, X. Wei, S. He, J. Huang and K. Pu, *Angew. Chem., Int. Ed.*, 2023, **135**, e202217339.
20 X. Sun, Y. Zhang, J. Li, K. S. Park, K. Han, X. Zhou, Y. Xu, J. Nam, J. Xu, X. Shi, L. Wei, Y. L. Lei and J. J. Moon, *Nat. Nanotechnol.*, 2021, **16**, 1260–1270.
21 Y. Zhang, X. Hou, S. Du, Y. Xue, J. Yan, D. D. Kang, Y. Zhong, C. Wang, B. Deng, D. W. McComb and Y. Dong, *Nat. Nanotechnol.*, 2023, **18**, 1364–1374.
22 Y. Sun, J. Sun, M. Xiao, W. Lai, L. Li, C. Fan and H. Pei, *Sci. Adv.*, 2022, **8**, eadd1106.
23 J. Zhang, B. Fan, G. Cao, W. Huang, F. Jia, G. Nie and H. Wang, *Adv. Mater.*, 2022, **34**, e2205950.
24 W. Yang, H. Deng, S. Zhu, J. Lau, R. Tian, S. Wang, Z. Zhou, G. Yu, L. Rao, L. He, Y. Ma and X. Chen, *Sci. Adv.*, 2020, **6**, eabd1631.
25 X. Xu, G. Deng, Z. Sun, Y. Luo, J. Liu, X. Yu, Y. Zhao, P. Gong, G. Liu, P. Zhang, F. Pan, L. Cai and B. Z. Tang, *Adv. Mater.*, 2021, 2102322.
26 Y. Min, K. C. Roche, S. Tian, M. J. Eblan, K. P. McKinnon, J. M. Caster, S. Chai, L. E. Herring, L. Zhang, T. Zhang, J. M. DeSimone, J. E. Tepper, B. G. Vincent, J. S. Serody and A. Z. Wang, *Nat. Nanotechnol.*, 2017, **12**, 877–882.
27 J. Lou, C. Meyer, E. B. Vitner, K. Adu-Berchie, M. T. Dacus, G. Bovone, A. Chen, T. To, D. A. Weitz and D. J. Mooney, *Adv. Mater.*, 2024, e2309860.
28 X. Hou, T. Zaks, R. Langer and Y. Dong, *Nat. Rev. Mater.*, 2021, **6**, 1078–1094.
29 Z. Xie, Y. C. Lin, J. M. Steichen, G. Ozorowski, S. Kratochvil, R. Ray, J. L. Torres, A. Liguori, O. Kalyuzhniy, X. Wang, J. E. Warner, S. R. Weldon, G. A. Dale, K. H. Kirsch, U. Nair, S. Baboo, E. Georgeson, Y. Adachi, M. Kubitz, A. M. Jackson, S. T. Richey, R. M. Volk, J. H. Lee, J. K. Diedrich, T. Prum, S. Falcone, S. Himansu, A. Carfi, J. R. Yates, J. C. Paulson, D. Sok, A. B. Ward, W. R. Schief and F. D. Batista, *Science*, 2024, **384**, eadk0582.
30 K. L. Swingle, A. G. Hamilton, H. C. Safford, H. C. Geisler, A. S. Thatte, R. Palanki, A. M. Murray, E. L. Han, A. J. Mukalel, X. Han, R. A. Joseph, A. A. Ghalsasi, M.-G. Alameh, D. Weissman and M. J. Mitchell, *Nature*, 2024, **637**, 412–421.
31 Y. Zhao, J. P. May, I. W. Chen, E. Undzys and S.-D. Li, *Pharm. Res.*, 2015, **32**, 3261–3268.
32 S. Landmann, A. Mühlethaler-Mottet, L. Bernasconi, T. Suter, J. M. Waldburger, K. Masternak, J. F. Arrighi, C. Hauser, A. Fontana and W. Reith, *J. Exp. Med.*, 2001, **194**, 379–391.
33 D. Y. Ma and E. A. Clark, *Semin. Immunol.*, 2009, **21**, 265–272.
34 A. Pitchaimani, T. D. T. Nguyen and S. Aryal, *Biomaterials*, 2018, **160**, 124–137.
35 Z. Liu, W. Zhang, H. Zhao, M. Sun, C. Zhao, J. Ren and X. Qu, *Angew. Chem., Int. Ed.*, 2024, **63**, e202411905.
36 M. Sun, Z. Liu, L. Wu, J. Yang, J. Ren and X. Qu, *J. Am. Chem. Soc.*, 2023, **145**, 5330–5341.
37 Y. Liu, W. Zhen, Y. Wang, S. Song and H. Zhang, *J. Am. Chem. Soc.*, 2020, **52**, 21751–21757.